Estimating wave orbital velocity through the azimuth cutoff from space-borne satellites

Justin Stopa, Fabrice Ardhuin, Bertrand Chapron, Fabrice Collard

To cite this version:

Justin Stopa, Fabrice Ardhuin, Bertrand Chapron, Fabrice Collard. Estimating wave orbital velocity through the azimuth cutoff from space-borne satellites. Journal of Geophysical Research. Oceans, 2015, 120 (11), pp.7616-7634. 10.1002/2015JC011275 . hal-04200762

HAL Id: hal-04200762
https://hal.science/hal-04200762v1

Submitted on 29 Sep 2023

AGU PUBLICATIONS

JGR

Journal of Geophysical Research: Oceans

RESEARCH ARTICLE

10.1002/2015JC011275

Key Points:

- The synthetic aperture radar spectral azimuth response mirrors the radial velocity of the scatters
- The azimuth cutoff compares well with buoys and models providing independent measurements
- Orbital wave velocities have important engineering applications

Correspondence to:
J. E. Stopa,
justin.stopa@ifremer.fr

Citation:
Stopa, J. E., F. Ardhuin, B. Chapron, and F. Collard (2015), Estimating wave orbital velocity through the azimuth cutoff from space-borne satellites, *J. Geophys. Res. Oceans*, *120*, 7616–7634, doi:10.1002/2015JC011275.

Received 28 AUG 2015
Accepted 26 OCT 2015
Accepted article online 30 OCT 2015
Published online 22 NOV 2015
Corrected 8 MAY 2018

This article was corrected on 8 MAY 2018. See the end of the full text for details.

Estimating wave orbital velocity through the azimuth cutoff from space-borne satellites

Justin E. Stopa[1], Fabrice Ardhuin[1,2], Bertrand Chapron[1], and Fabrice Collard[3]

[1]Ifremer, Laboratorie d'Oceanographie Spatiale, Plouzane, France, [2]Ifremer, Laboratorie de Physique des Oceans, Plouzane, France, [3]Ocean Data Lab, Plouzane, France

Abstract It has been long accepted that ocean wave conditions recorded from synthetic aperture radar (SAR) aboard satellites resolve large scale swells. SARs make use of its displacement to achieve fine resolution; however the random surface motions can reduce its nominal azimuthal resolution. Accordingly, the SAR spectral azimuth response mirrors the probability distribution of the radial velocity component of the scatters. This effect, quantified in a measure called the azimuth cutoff, is estimated by defining a scale based on the fitting of a Gaussian function to the radar cross section azimuth spectrum. The independent measure provides additional sea state information related to the root mean square surface orbital wave velocity. We use data recorded from the European Space Agency's ENVISAT advanced SAR in the C-band spanning its lifetime 2003–2012. Our purpose is to first establish the validity of the azimuth cutoff using both colocated buoys and modeled wave data. Some systematic biases are corrected using other SAR derived parameters, improving the accuracy of the estimate. Despite our efforts, errors exist in the presence of swell, extreme wind waves, and related to the wave direction. Under the majority of the sea states the parameter is well behaved. As a final point, applications using the wave orbital velocities are described in terms of diagnosing a spectral wave model and the wave climate. As illustrated, the returned radar signal provides useful sea state information that resolves wind speeds, wave orbital velocities from the wind waves, and swells.

1. Introduction

Remotely sensed wind and wave data provide a vital source of marine observations that respond to the growing need for accurate information at sea. One of the most powerful applications of the remotely sensed data is the extensive space-time information that might not be available with in situ observations. It is well established that observed wave-like features contained in images of ocean surface from synthetic aperture radars (SAR) are a valuable source of information [*Alpers et al.*, 1981; *Hasselmann et al.*, 1985a]. For communities interested in ocean waves, the two dimensional spectrum is the often most useful. Yet in practice the extraction of an accurate wave spectrum is not direct and mostly limited by the nonlinear mapping induced by random motions of the ocean surface [e.g., *Kerbaol et al.*, 1998]. This affects the nominal along-track (azimuthal) resolution. The limit is often referred to as the azimuth cutoff and can then independently be estimated from the azimuth spectral response of the SAR radar cross section. It is our purpose to demonstrate the merit of using the azimuth cutoff as a measure of the wave orbital velocity standard deviation. The wave orbital velocity is particularly relevant for ocean engineering applications because it is used to calculate forces on oceanic structures. In the engineering community, it is still common practice to compute wave forces using the Morison Equation, where the orbital wave velocity is usually the most difficult quantity to approximate.

Sea surface displacements introduce Doppler shifts which distort the phases of returned radar signal and create constructive or destructive effects. In the case of swell, the waves have a strong space-time correlation and result in constructive velocity bunching [*Swift and Wilson* 1979; *Ardhuin et al.*, 2015]. In the case of dominant wind seas, velocities are more random. The SAR processing becomes destructive and results in an apparent blurring. This creates a distortion in the direction of satellite motion and produces the azimuth cutoff. In practice the cutoff can be thought of as a scale representing a lower limit of waves that can be adequately resolved by the SAR imaging [*Alpers and Bruning*, 1986]. The quantity is proportional to the range-to-platform velocity ratio R/V described by *Beal et al.* [1983] and is theoretically related to the total variance of the vertical wave velocities [e.g., *Lyzenga* 1986].

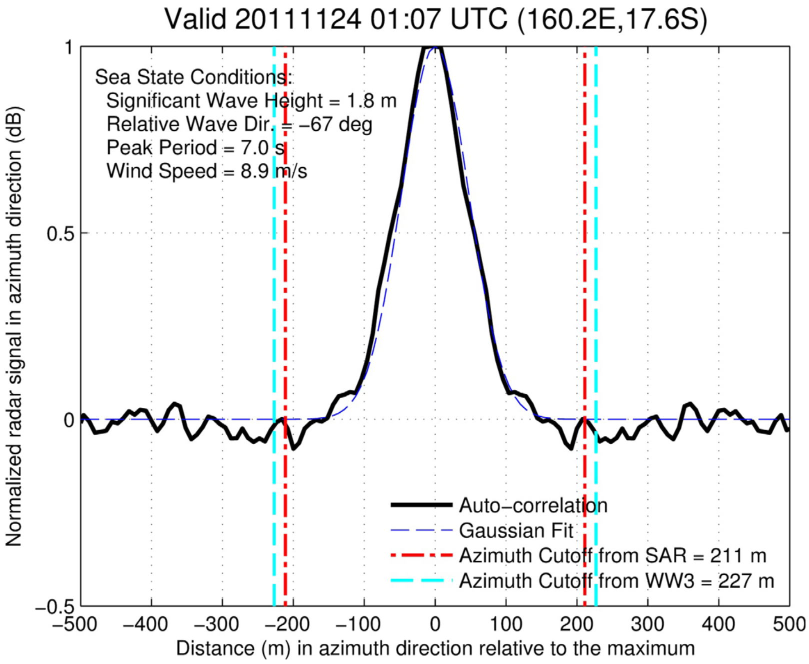

Figure 1. Example of azimuth cutoff estimation. Solid black line represents the auto-correlation function of the maximum pixel along the azimuth direction, the dashed blue line represents the Gaussian fit, the red vertical dashed-dotted line is the cutoff estimated from SAR, and the cyan vertical dashed line is the cutoff estimated from WW3. The wind and dominant wave conditions are given in the top-left corner.

The azimuth cutoff has not received much attention as a useful sea state parameter. It is our focus to establish its accuracy, investigate the errors, and demonstrate its physical structure across the oceans. Once the validity is established, the more relevant and useful parameter, the wave orbital velocity, can be estimated. We make use of data measured from ENVISAT's advanced synthetic aperture radar (ASAR) which operates in the C microwave band throughout this study. The satellite was launched in November 2002 and operated until April 2012 offering a near continuous and extensive global data set. The level 2 product provided by European Space Agency's (ESA) uses the methodology described in *Chapron et al*. [2001] to estimate wave spectra from the SAR images using no outside information.

The paper is organized as follows, section 2 describes the data sets with details of the derived SAR quantities, in situ data from buoys, and modeled wave data. Section 3 establishes the accuracy heavily relying on in-situ buoy measurements. Here the partitioned wave errors from the SAR spectra are analyzed through the azimuth cutoff. Since the colocated buoy-SAR data set is limited we extend the comparison to wave information generated by WAVEWATCH III (WW3) [*Tolman and the WAVEWATCH III ® Development Group*, 2014]. The use of the wave model provides a robust data set to explain the spatial errors globally. To finish we illustrate the advantage of spatial coverage to diagnosis WW3's average wave period and then provide a brief description of the wave climate using the orbital velocity in section 4. A discussion and conclusions follow in section 5.

2. Data Sets and Methods

2.1. ENVISAT Wave Mode ASAR Data

The SAR data recorded from ENVISAT are published by the GlobWAVE project and are provided by ESA. ENVISAT operated for approximately 10 years and provides an extensive global data set. The radar incidence is approximately 23° from nadir and consequently the radar cross section is still strongly influenced by the waves [*Quilfen et al*., 2004a]. The cutoff is estimated by minimizing the standard error of a Gaussian function fitted to the auto-correlation of the radar cross section orientated in the azimuth direction [*Kerbaol et al*., 1998]. An example is given in Figure 1. The Gaussian function matches the autocorrelation well under typical sea state conditions (i.e., moderate winds and waves). This method generally gives reasonable estimates compared to empirical extrapolations that can be based on its dependence on significant wave heights [*Beal et al.*, 1983], long wave orbital motions [*Tucker*, 1985; *Hasselmann et al.*, 1985a], and wind speed [*Elfouhaily et al.*, 1997]. Assuming linear waves, *Lyzenga* [1986] expressed the azimuth cutoff as

$$\lambda=\pi\frac{R}{V}\sqrt{\int_{0}^{\infty}\omega^2F(f)df} \tag{1}$$

where *R*/*V* is the range to platform ratio and is equal to 120 s for ENVISAT, $\omega=2\pi f$, and *f* is the wave frequency. From this relation, the azimuth cutoff is proportional to the orbital wave velocity denoted by the quantity underneath the radical and is referred to as the second moment of the wave spectrum (*m*2).

The ENVISAT level 2 product includes a wave spectrum derived from the cross correlation functions between different SAR detected scenes taken at (three) different times during the integration dwell-time. Based on numerical simulations, look-up tables have been derived to compare the fully nonlinear SAR mapping effects on prescribed wind-sea spectra [e.g., *Elfouhaily et al.*, 1997] with the measurements. Once adjusted and removed, a quasi-linear approximation is then implemented to estimate the wave spectra [*Chapron et al.*, 2001]. This approximation works well for ocean swells that are characterized by small steepness [*Collard et al.*, 2009]. The directional wave spectra have a resolution of 10° and a logarithmic distribution of 24 wave numbers from 30 to 800 m with a 7% increment. Partitioned wave quantities of significant wave height, peak frequency, and dominant direction are calculated from the wave spectra using a watershed method to separate the different wave systems. An adaptation of *Portilla et al*. [2009] is implemented by using the same kernel, but only applied once due to the smooth nature of the derived SAR spectra. ENVISAT is also equipped with a nadir-looking altimeter from which significant wave heights are estimated. These data have been quality controlled by *Queffeulou and Croizé-Fillon* [2015] and *Sepulveda et al*. [2015].

2.2. Wave Buoys

Buoy measurements from the National Oceanographic Data Center (NODC) and the Coastal Data Information Program (CDIP) networks provide quality controlled directional wave data from their networks. To assess the SAR data quality from ENVISAT, colocations are limited to 100 km and result in time differences less than 30 minutes. Directional wave spectra are created from the five frequency spectra recorded by buoys using the maximum entropy method (MEM) [*Earle et al.*, 1999]. The NODC buoys resolve frequencies of 0.485 Hz while the CDIP buoys resolve a slightly higher frequency at 0.58 Hz. However the accuracy at these higher frequencies becomes questionable therefore we truncate the spectra at 0.4 Hz and 0.5 Hz for the NODC and CDIP buoy respectively [e.g., *Vandemark et al.*, 2005]. Buoy spectra are naturally noisy, so they are smoothed in time using 3 hour running mean and then are interpolated to match the SAR spectral resolution. The averaging in time and spectral space results in sufficiently smoothed buoy spectra for further analysis with the SAR data.

2.3. Numerically Generated Wave Quantities

Wave data are generated using the spectral wave model, WW3, version 4.18. WW3 integrates the spectral wave action equation in space and time, with discretized wave numbers and directions. Conservative wave processes, represented by the local rate of change and spatial and spectral transport terms are balanced by the nonconservative sources and sinks. The global model uses a grid of 0.5° resolution in longitude and latitude with a spectral grid composed of 24 directions and 32 frequencies exponentially spaced from 0.037 to 0.7 Hz at an increment of 10 percent. All wave hindcasts are forced by winds from the Climate Forecast System Reanalysis (CFSR) of *Saha et al*. [2010, 2014]. Ice concentrations are provided by the CFSR and iceberg distributions of *Ardhuin et al*. [2011]. Subgrid features smaller than the 0.5° are accounted for by apportioning the energy [*Tolman* 2003a, 2003b; *Chawla and Tolman*, 2008]. Details regarding the physical parameterizations are explained by *Ardhuin et al*. [2010] and refined by *Rascle and Ardhuin* [2013]. *Stopa et al*. [2015] show the wave orbital velocity compares very well with buoys offering a means to robustly identify errors from SAR. On average percent biases of the model are less than 8%, have correlation coefficients larger than 0.9, scatter index of 0.10, root mean square error of 0.6 m, and match the variability of the buoy observations reasonably well.

3. Results

Analysis of the azimuth cutoff and its relationships between the wind speeds, wave age, fetch, and directionality aspects have been reported by *Kerbaol et al*. [1998] for ERS-1/2 SAR measurements. Despite these efforts, the

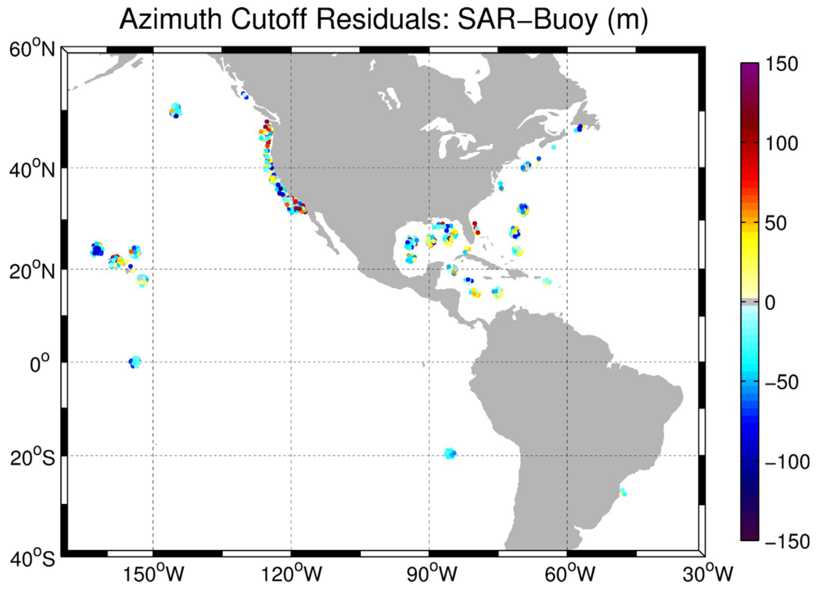

Figure 2. Spatial location of colocated buoys the colors denotes the azimuth cutoff residuals (SAR-Buoy) after the empirical correction.

validity of azimuth cutoff has not been established with any vigor so we proceed with making the comparison to buoys and the modeled wave data. To ensure quality measurements free from contamination due to the presence of ships, slicks, sea ice or islands, the normalized variance of the radar cross section is limited within the range of 1–1.5%. In addition, abnormally small significant wave heights less than 0.25 m are not included in the analysis. For the entire ENVISAT data set (December 2002 to April 2012) there are a total of 3790 colocated two-dimensional spectra with sufficient data utilizing both the NODC and CDIP networks. The buoys are located in deep and shallow water of the Pacific Ocean, Atlantic Ocean, Caribbean Sea and Gulf of Mexico shown in Figure 2.

3.1. Wave Directionality and High Frequency Wave Corrections

To appropriately compare the azimuth cutoff from SAR to the buoy and wave model, the geometry effects from the satellite orientation must be considered. The spectrum is rotated in the along-track direction, α, and effect of the incidence angle, β, measured from nadir is removed. Let u, v, and w denote the east-west, north-south, and vertical directions of the wave orbital velocities, then the variance of velocity, μ_o, directed toward the satellite can be written

$$\langle {\mu_o}^2\rangle = \langle w^2\rangle \cos^2\beta + \left(\langle u^2\rangle \cos^2\alpha + \langle v^2\rangle \sin^2\alpha - 2\langle uv\rangle \cos\alpha \sin\alpha\right)\sin^2\beta. \quad (2)$$

The variance of each wave orbital velocity can be related the wave spectrum $E(f,\theta)$ where θ is the wave direction

$$\langle u^2\rangle = \int_0^\infty E(f,\theta)(2\pi f)^2 \cos^2\theta \, df d\theta \quad (3a)$$

$$\langle v^2\rangle = \int_0^\infty E(f,\theta)(2\pi f)^2 \sin^2\theta \, df d\theta \quad (3b)$$

$$\langle w^2\rangle = \int_0^\infty E(f,\theta)(2\pi f)^2 \, df d\theta \quad (3c)$$

$$\langle uv\rangle = \int_0^\infty E(f,\theta)(2\pi f)^2 \sin\theta \cos\theta \, df d\theta. \quad (3d)$$

A analogous azimuth cutoff from the buoy or wave model is estimated using equation (1)

$$\lambda_{est} = \pi \frac{R}{V} \sqrt{\langle {\mu_o}^2\rangle}. \quad (4)$$

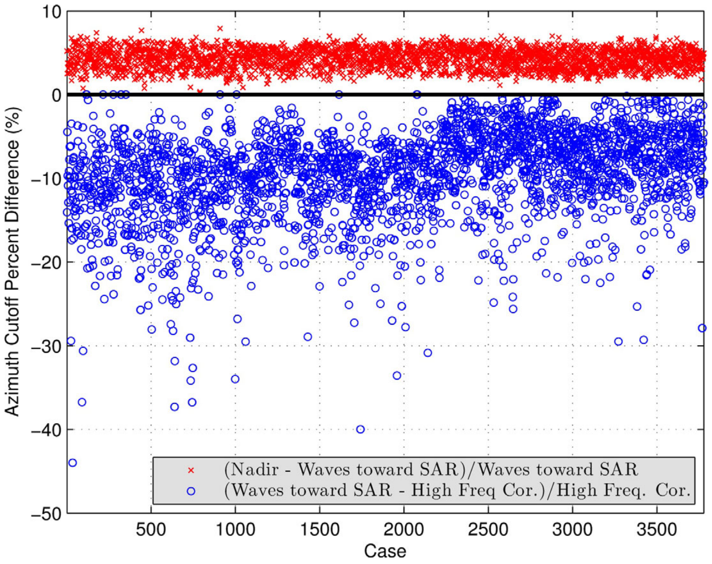

Figure 3. Geometric and high frequency tail corrections used to calculate an equivalent azimuth cutoff from the buoy spectra. The red "*X*'s" denote the geometric corrections including the satellite's track and the incident angle to estimate the wave orbital velocity directed toward the satellite radar. The blue "*O*'s" denote the high frequency wave correction assuming the wave energy decays with the power -5.

The red *X*'s in Figure 3 show the effect of the satellite's geometry are minimal. The comparison is relative to the waves directed in the nadir direction ($\beta=0°$). The percent difference is within 2–7% of the actual value. *Kerbaol et al*. [1998] found the ratio between the cutoffs estimated from the azimuth and range direction to be less than 5%. Therefore assuming the satellite is directed in the nadir direction ($\beta=0°$) is a good first approximation to estimate the root mean squared vertical velocity. The incidence angle for ENVISAT is 23° thus it is not surprising the difference is small.

High frequency waves can strongly influence the orbital wave velocity since the integration limits of equation (3) extend to infinity and the frequency is squared. Neither the buoys nor wave model are able to adequately resolve these small scale waves. The upper frequency limit is 0.4 Hz for the NODC buoys, 0.5 Hz for the CDIP buoys, and 0.7 Hz for our WAVEWATCH simulations. We approximate the contribution from these high frequency waves by assuming a cascade of energy with the parametric shape of f^{-5}. The power -5 is applicable for a large range of sea states and is created by the balance between wave breaking and growth [*Pierson and Moskowitz*, 1964; *Alves et al*., 2003]. The high frequency wave contribution is calculated by scaling the energy at the highest resolved frequency, f_o, by f^{-5} as

$$E_{hf}(f)=\int_{f_o}^{\infty} E(f_o)(f/f_o)^{-5}df. \tag{5}$$

The velocities in equation (3) are corrected using this approximation and the relative difference is depicted in Figure 3 by the blue circles. If the high frequency components are ignored the calculated azimuth cutoff will be underestimated by 5–15% with extreme differences exceeding 30%. These large differences are produced by events with small values of the azimuth cutoff ($<$ 150 m) and coupled with actively growing wind seas. For example, the outlier with a value of -46% has an azimuth cutoff of 85 m and becomes 155 m when the high frequency components are included. Therefore the high frequency wave components must be considered. These buoy locations represent a subset of the global wave conditions and the effect from the high frequency components are expected to play a more important role in the Westerlies which is dominated by wind seas [*Chen et al*., 2002; *Semedo et al*., 2011]. Throughout the remainder of the study both the geometric and high frequency tail contributions are included unless otherwise noted.

3.2. Validation With Buoys

Figure 4 shows the comparison using all colocations between the buoys and ENVISAT. The colors denote the wind speed estimated from the satellite and the size of the circles denotes the significant wave height from the buoy to give an indication of the environmental conditions. There is a clear relationship: the azimuth cutoff increases with wave height and wind speed. The left plot shows the data directly computed from the Gaussian fit of the radar cross section and the right plot shows the results after an empirical fit and will be discussed shortly. Error statistics are summarized in Table 1. When the wind speed (U10) and significant wave heights (*Hs*) are small (U10 $<$ 3 m/s and *Hs* $<$ 1 m) there is decreased performance and an overestimation. One possible explanation for the poor estimation under calm wind conditions is that there might not be enough sea surface roughness to create a sufficient contrast to adequately resolve the scene. On the

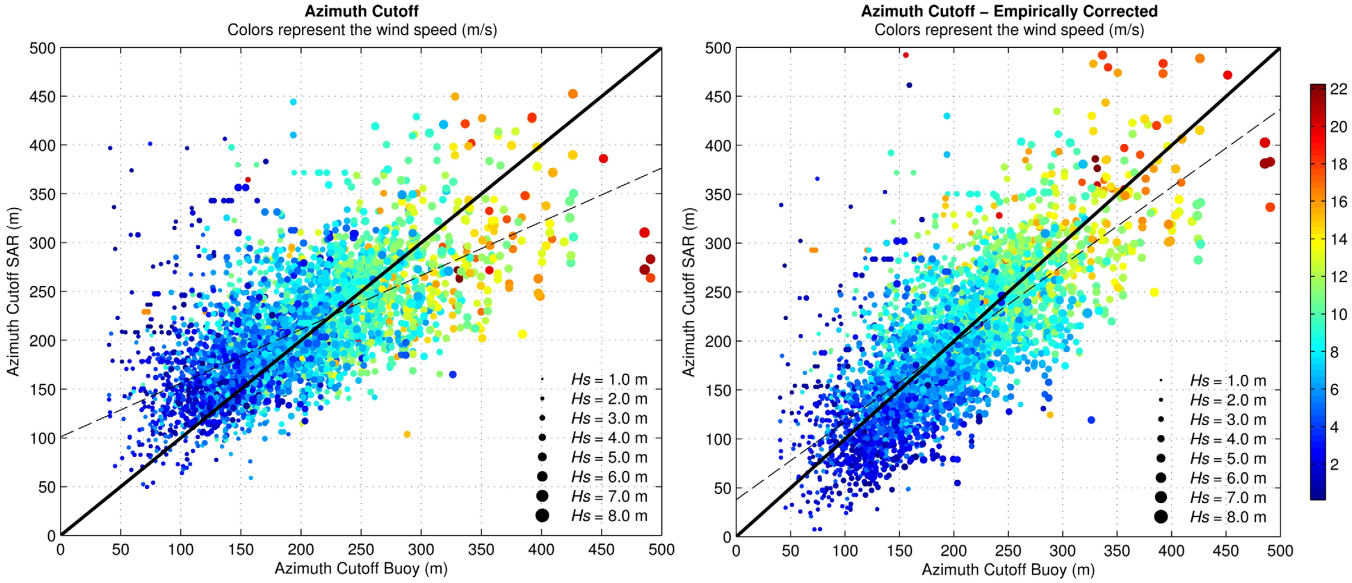

Figure 4. Comparison of azimuth cutoff from (left) the buoy and SAR before and (right) after the empirical correction. The colors denote the wind speed from SAR and the size of the markers denotes the significant wave height from the buoys.

other hand, the azimuth cutoff is underestimated when the wind speed and wave heights are large ($U10 > 15$ m/s and $Hs > 5$ m). These conditions correspond to wind seas and are characterized by large steepness which might cause problems fitting the smooth Gaussian function.

The error dependencies of the azimuth cutoff residual (SAR-buoy) are summarized in Table 2. The correlation coefficients and least-squared linear regression slopes quantify the strength of the relationship. The errors are independent of the buoy locations shown by the small correlation coefficients for longitude, latitude, and the distance between the colocated points. There is a statistically significant relationship at the 99.9% level with the SAR derived quantities from the radar signal: normalized radar cross-section (σ_0), normalized variance (*nv*), and wind speed (U10). The wave age, defined by the ratio of peak wave phase speed to wind speed has a weaker relationship than solely using the wind speed. The buoy derived quantities of the significant wave height and the mean squared slope (*mss*) have the strongest relationship of any variable tested. The mean squared slope proportional to a fourth order moment of the wave spectrum is very sensitive to the high frequency wave components explaining 22% of the residual variance. It is not surprising the mean squared slope is most strongly related to the azimuth cutoff since the relationship is used to derive wave periods from sigma naught of satellite altimeters [e.g., *Gommenginger et al.*, 2003]. Notice that the average wave period which is strongly related to the wave orbital velocity has only a weak relationship

Table 1. Azimuth Cutoff Error Metrics of the Colocated SAR-Buoy Measurements[a]

Category	N	Bias m	NRMSE	SI	Cor	NSTD
All Data	3790	15.99 (−0.35)	12.79 (11.39)	0.29 (0.27)	0.62 (0.74)	0.88 (1.09)
Wind Speed Sensitivity						
$U10 < 3$ m/s	450	51.49 (−3.74)	35.47 (28.00)	0.59 (0.58)	0.11 (0.08)	1.63 (1.57)
3 m/s $< U10 <$ 15 m/s	3267	12.17 (−0.52)	13.31 (12.24)	0.25 (0.24)	0.64 (0.72)	0.91 (1.06)
$U10 > 15$ m/s	71	−33.26 (29.90)	22.32 (21.82)	0.28 (0.27)	0.39 (0.41)	0.80 (0.81)
Significant Wave Height Sensitivity						
$Hs < 1$ m	475	49.94 (17.67)	53.57 (40.19)	0.61 (0.56)	−0.04 (0.13)	1.88 (1.85)
1 m $< Hs <$ 5 m	3272	11.99 (−2.57)	15.21 (14.27)	0.26 (0.25)	0.59 (0.70)	0.93 (1.16)
$Hs > 5$ m	43	−54.95 (−30.21)	54.26 (43.94)	0.26 (0.23)	−0.05 (0.28)	1.35 (1.44)
Wind Speed and Significant Wave Height Sensitivity						
$Hs < 1$ m; $U10 < 3$ m/s	158	81.69 (30.25)	103.81 (72.73)	0.92 (0.87)	0.01 (0.01)	3.45 (3.26)
$1 < Hs < 5$ m;$3 < U10 < 15$m/s	3244	12.09 (−3.65)	14.47 (13.42)	0.26 (0.24)	0.60 (0.71)	0.93 (1.13)
$Hs > 5$ m; $U10 > 15$ m/s	16	−84.10 (−19.65)	82.85 (56.99)	0.24 (0.21)	−0.34 (−0.14)	1.49 (1.39)

[a] The values in parentheses represent values after the empirical correction is applied.

Table 2. Correlation Coefficients and Least Square Linear Regression Coefficients Between the Azimuth Cutoff Residual (SAR-Buoy) and the Various Parameters[a]

Parameter	Source	Correlation Coefficients	Slope
Distance to buoy (km)	N/A	0.02	0.04
Longitude (°)	SAR	−0.01	−0.01
Latitude (°)	SAR	0.02	0.13
Wind speed (m/s)	SAR	−0.34*	−5.58
Normalized variance (%)	SAR	+0.31*	181.86
Sigma naught (dB)	SAR	−0.31*	−9.29
Wave age	SAR	+0.19*	1.37
Significant wave height (m)	Buoy	−0.36*	−20.84
Average wave period (s)	Buoy	+0.12*	4.85
Mean squared slope (%)	Buoy	−0.47*	−35.74

[a] A "*" represents statistical significance at the 99.9% confidence interval.

to the residual errors. This suggests that our estimation of the azimuth cutoff describes the wave orbital velocity to a leading order.

The dependencies of the residuals relative to the wave direction orientated along the satellite track are given in Figure 5. For each colocated spectra the dominant wave partitions are matched by minimizing the spectral distance. The top and middle plots show the residual azimuth cutoff (SAR-Buoy) versus the partitioned wave height. The bottom plot presents the data density showing most of these occasions are close to the range direction (90° or 270°). The SAR transform tends to shift the waves toward the range direction slightly exaggerating this effect. When waves are directed in the azimuth direction the velocity bunching mechanism creates a coherent signal and the auto-correlation function will contain wave information. Despite this distortion, the algorithm performs reasonably well with only relatively small biases near 0° and ±180°. Notice that the standard deviation of the cutoff residual is approximately 75 m for waves directed along the track (0°, ±180°) compared to 125 m when waves are directed in the range (±90°). Therefore, on average, a higher positive bias occurs when waves are directed in the range direction. This is due to the fact that the radar signal along the azimuth direction contains information from the crest spreading of waves directed in the range direction and makes the Gaussian fit more difficult. In the SAR processing, energy is superficially added to the wave spectrum with an amount proportional to the energy unresolved by the cutoff and creates the positive bias in wave heights directed in the range direction. Therefore caution must be taken when waves are directed in the range (or close to) and it is expected that an improvement in the azimuth cutoff will result in improved performance of the partitioned wave quantities.

From the relationships given in Figure 4 and Table 2, empirical corrections can be implemented to improve the data quality. In order to keep the azimuth cutoff as a strictly independent measure, only parameters directly derived from SAR are used. Therefore the different combinations of wind speed, normalized variance, and sigma naught are explored. It is concluded that using all three variables yielded the best improvement in the data quality (not shown). The linear bias correction from the multi-variant least squared fit is approximated by

$$\lambda_{bias}=-10(U10)+60(nv)+5(\sigma_0)-45 \tag{6}$$

rounded to the nearest whole number. The wind creates the largest variation ranging 220 m while the normalized variance varies 30 m and sigma naught varies 60 m. It is important to note that all of these quantities are all derived from the mapped radar cross section and are interrelated. The wind speed comes from the geophysical model function and the effect of using σ_0 and the normalized variance is equivalent to adding higher order components of the radar signal. The range, average, median, and standard deviation of the bias correction are 200 m, 16.3 m, 18.3 m, and 26 m. The values given in the parentheses in Table 1 demonstrate improved performance for all error metrics.

Figure 6 shows the relationship between the residuals and the selected SAR variables before and after the empirical correction. The top and middle plots show scatterplots, averages, standard deviations, and linear fit while the bottom plots show the number of data in discretized bins. The top plots are the original data and the middle plots show the data after the empirical correction ($\lambda_{\mathrm{cor}}=\lambda-\lambda_{\mathrm{bias}}$). Before the correction, the cutoff residuals have decreasing trends with an over estimation at low values ($<$150 m) and under estimation at high values ($>$300 m). The same decreasing trends exist between the wind speed and sigma naught. The normalized variance shows an increasing trend and has very minimal biases in the range of 1.05–1.2 where the majority of the data lies. After the correction, the slopes of the fitted lines reduce and the skill of the azimuth cutoff generally improves and removes the bias. The normalized root mean square error, scatter index, and correlation coefficients improve but only slightly. Figure 4 (right) shows the empirically corrected results demonstrating the improvement especially when the wind speeds and wave heights are

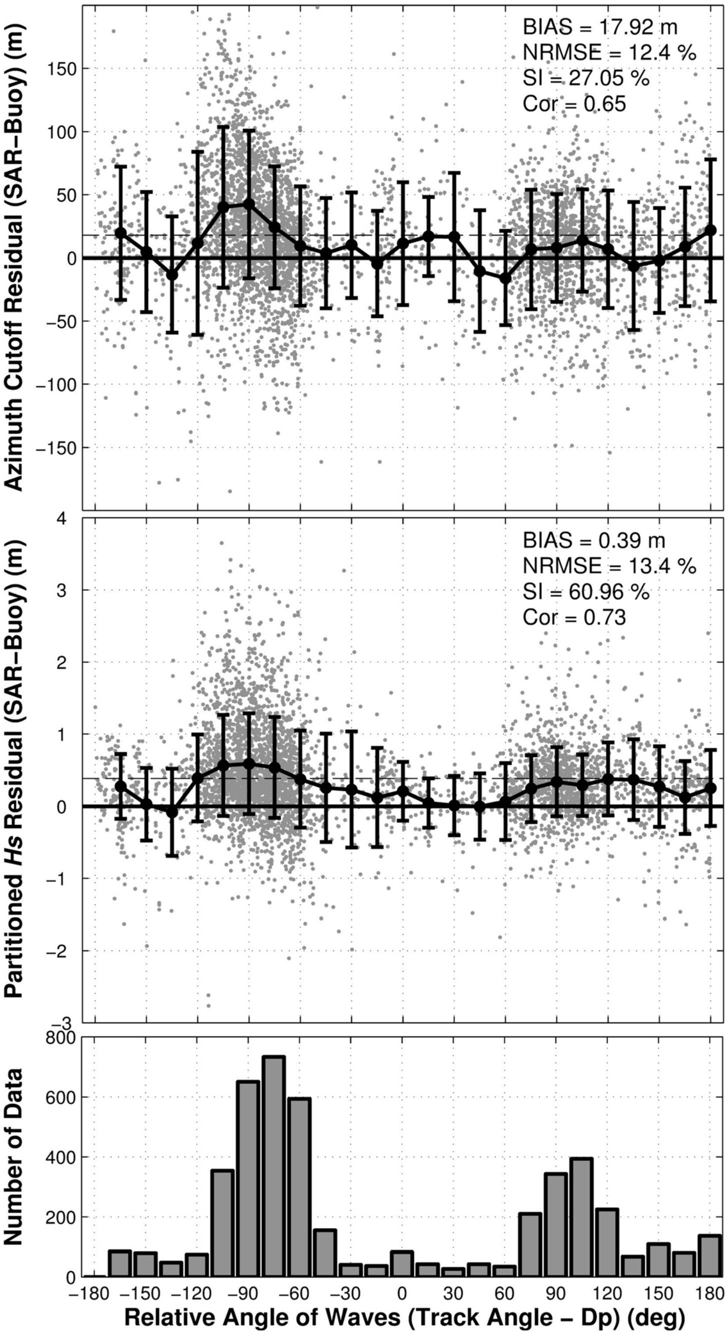

Figure 5. Dependence of the residuals (SAR-Buoy) of the (top) azimuth cutoff and (middle) partitioned wave height with respect to the relative direction between the dominant waves and the satellite track angle in 10° bins. The large black circles denote the binned mean and the error bars denote 1 standard deviation. (bottom) The dashed lines shows the least squared linear trend, and the number of data points is given.

large but exasperates the underestimation for small azimuth cutoffs. The corrected values are heavily weighted on the wind speed and the majority of the data lies within the 5–10 m/s range. Under these wind conditions, the azimuth cutoff is well approximated and the empirical correction is only able to improve the bias while the scatter indices remain the same. The azimuth cutoff biases for the low ($<$ 3 m/s) and high ($>$15 m/s) wind regimes have similar RMSEs and precision errors before and after the correction (Table 2).

Figure 2 shows the residual of all colocated buoys from both the NODC and CDIP networks after the empirical correction. No clear spatial biases can be determined from this depiction but the largest discrepancies occur on the west coast of the United States and a buoy northwest of Hawaii. Several instances of overestimation exceeding 100 m can be seen in buoys offshore of South California and Washington. Otherwise differences are consistently less than 75 m.

3.3. Verification With WAVEWATCH III

Due to the limited nature of the colocated buoy-SAR data set, the azimuth cutoff estimated from the WW3 hindcast is compared to the corrected SAR data. The wave model has the ability to cover the globe and expands the analysis to greater than 10^6 colocated spectra for 2011. Figure 7 shows the residual scatterplots of colocated data from WW3 and SAR for 2011. Due to the large amount of colocated points (636,189), the data are plotted by density on logarithmic scale with the contours representing 95%, 75%, 50%, and 10% of the data set. Some nonlinear effects are seen in relation to the azimuth cutoff where an over estimation exists when the cutoff is less than 125 m and an underestimation exists for the largest values greater than 450 m. Otherwise the majority (95%) of all data pairs have residuals less than 75 m and standard deviations less than

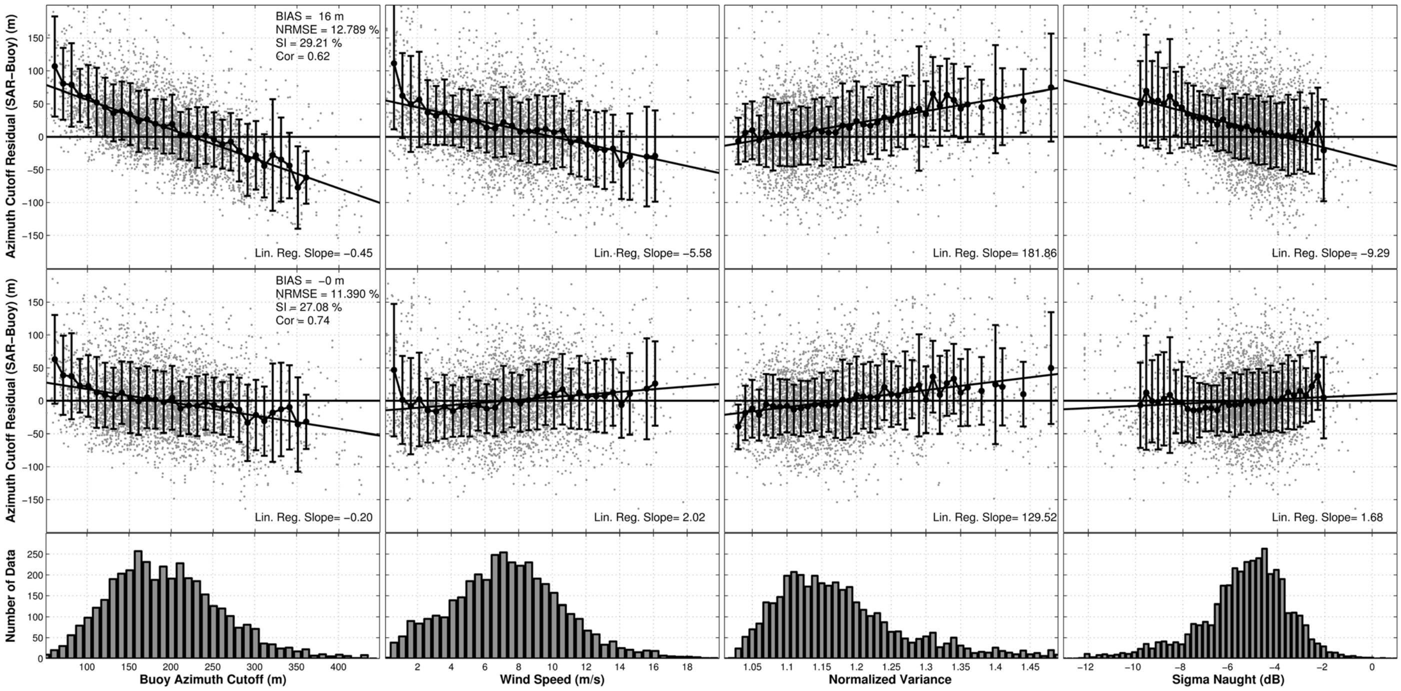

Figure 6. Dependence of azimuth cutoff residual (SAR-Buoy) on the azimuth cutoff (first column), SAR wind speed (second column), normalized variance (third column), and sigma naught (fourth column). Before the correction (top row) and after the correction (middle row) scatterplots, averages, standard deviations, and linear trends are given. The number of data points is presented in the bottom row.

50 m. Despite the small biases, larger errors exist; especially when the azimuth cutoff is less than 50 m. For these cases the predicted values can be 2–3 times larger. Typical of any narrow banded random process the statistical distribution of the azimuth cutoff is similar to the Rayleigh distribution [*Longuet-Higgins*, 1952].

Residuals with respect to the depth, significant wave height, wave age, and mean squared slope are given in Figure 8. There is virtually no trend with respect to the depth demonstrating its applicability to various sea states. Therefore SAR is able to adequately observe wave orbital velocities in coastal shallow water regions, routinely where ocean engineering practices take place. For additional information of wave quantities estimated from SAR in coastal regions refer to *Collard et al*. [2005]. Similar to the buoy comparison, the wave height and mean squared slopes have the largest influence on the residuals, characterized by the same functionality as the azimuth cutoff errors in Figure 7. The effects of swells are mainly causing the errors when the mean squared slopes and wave heights are small (0.2% and <1 m). When the mean squared slope is large (i.e., steep waves), the azimuth cutoff is underestimated. The wave age generally has the same functional shape as the significant wave height because the bias correction removes the wind effect making the deviation less dramatic. In summary, the empirically corrected azimuth cutoff residuals have minimal trends related to the wind speed, normalized variance, sigma naught, depth, and wave age demonstrating its robust performance. However the effect of swells and large wind waves are not well modeled.

Figure 9 shows spatial distribution of the outliers greater than 200 m, the scatter index, and the correlation coefficients. The outliers in the top plot show only a few instances of SAR underestimating the waves, but there are numerous instances of over estimation. These locations are clustered in the North Pacific, western Pacific near Japan, and along the Equator near Madagascar, Papua New Guinea, and West Africa. After removal of these outliers the variability of SAR matches WW3 reasonably well but has the same problematic areas in the middle plot. In the Southern Hemisphere and the trade wind regions the variability is generally less 15% but in the Northern Hemisphere there are slightly larger scatter indices of $\sim$20%. The largest variability ($>$25%) between the two data sets occurs in the North Pacific and near landmasses especially near Micronesia and Japan. The same spatial inaccuracies of the extreme residuals and scatter indices suggest

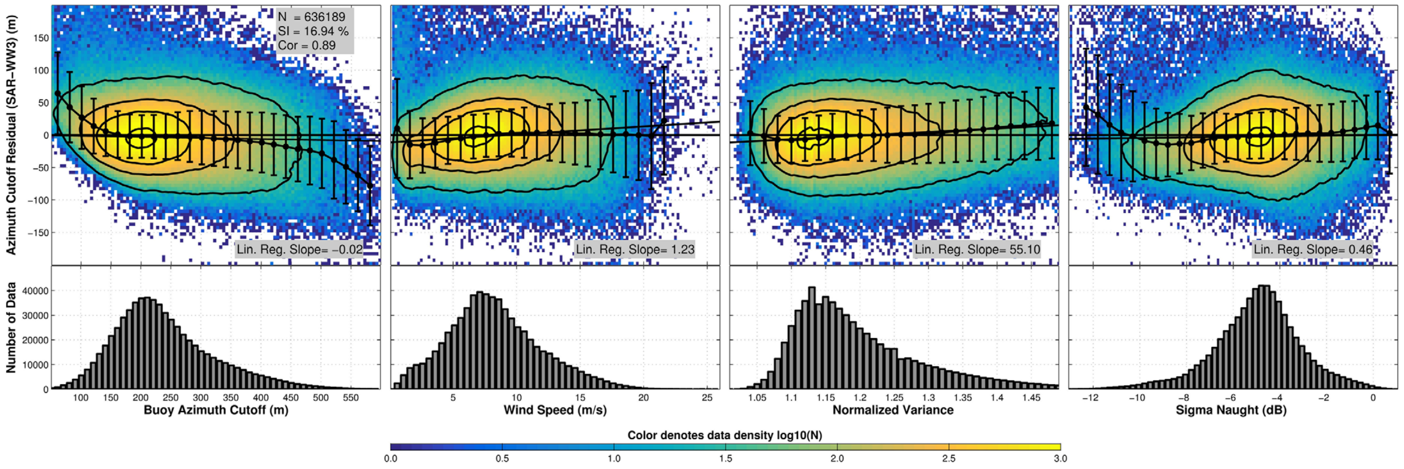

Figure 7. Same as Figure 6 except for SAR-WW3 residuals using colocated data for 2011 calculated after the correction is applied. The color bar shows the data density of each discrete bin on a logarithmic scale. The contours denote 95, 75, 50, and 10% of the data set.

systematic errors in these regions. These problematic areas have relatively small values of azimuth cutoff (<150 m) and the influence of swell is most likely causing the extreme overestimation [e.g., *Kerbaol et al.*, 1998]. Despite these errors the correlation coefficient (*r*) is well matched (>0.85) with only the area near the Equator having poor performance. In short, the azimuth cutoff has errors but it is a reasonable predictor of the sea state.

4. Applications

4.1. Model Diagnostic

So far we have used WW3 as a means to demonstrate the performance of the remotely sensed data with statistics. Now we make use of the data recorded from the SAR and the altimeter aboard ENVISAT to assess the performance of WW3. Figure 10 shows the comparison between WW3 and the satellite assessing both the significant wave height, and orbital wave velocity for 2011. The azimuth cutoff outliers with differences larger than 200 m are removed in this analysis. The significant wave height proportional to the zeroth moment (*m*0) of the wave spectra from the altimeter and WW3 are shown in the top-left plot. The wave model overestimates in the extra tropics and underestimates in the low-latitudes (25°S–25°N). There is an enhanced underestimation in the western Pacific. This bias might be due to insufficient subgrid blocking and lack of wave reflection from islands [*Ardhuin et al.*, 2010]. In general, the biases are less than 40 cm and

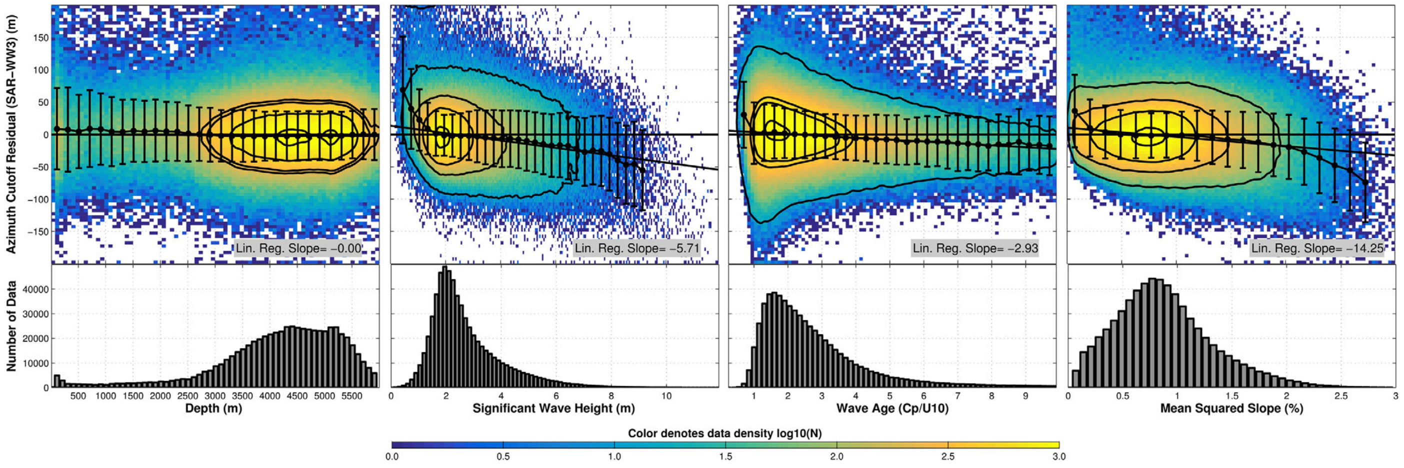

Figure 8. Same as Figure 7 comparing the SAR-WW3 azimuth cutoff residuals to the depth, significant wave height, wave age, and mean squared slope using colocated data for 2011.

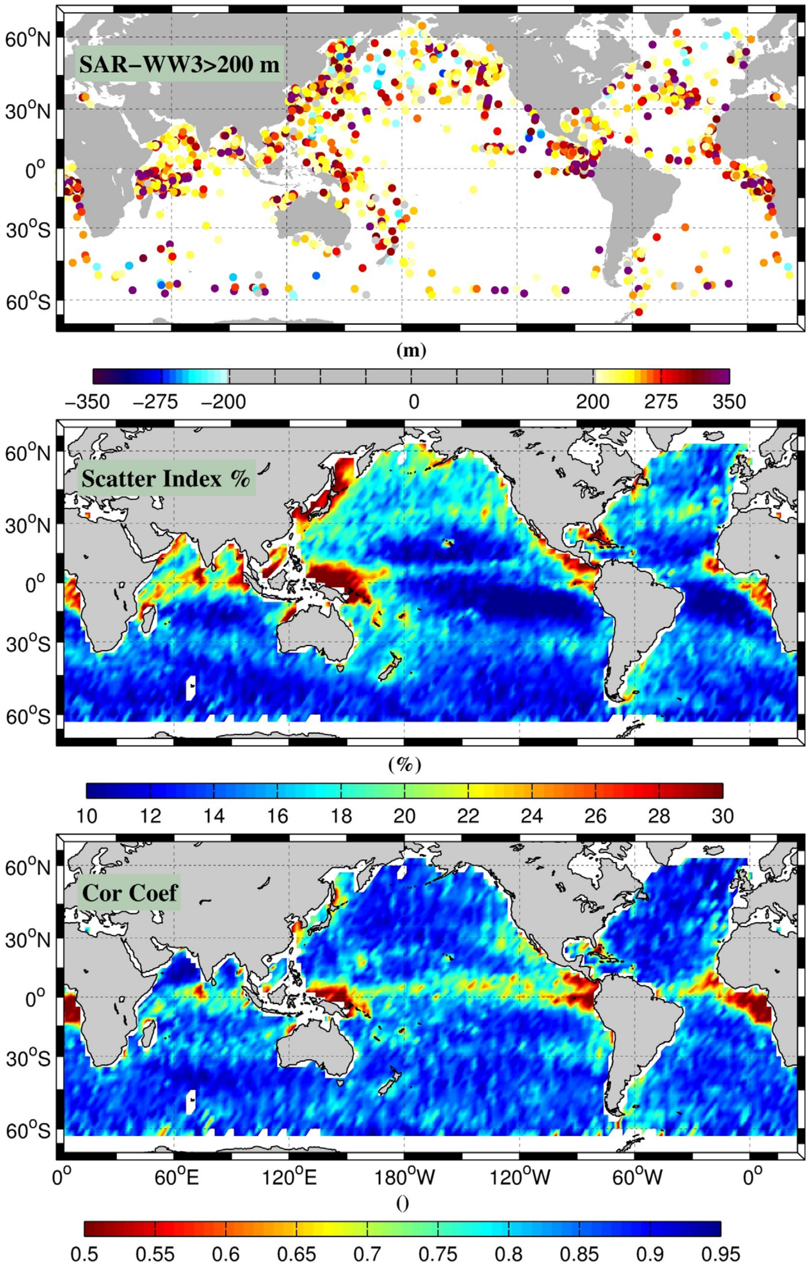

Figure 9. (top) Azimuth cutoff outliers SAR-WW3 (>200 m), (middle) scatter index and (bottom) correlation coefficient between SAR and WW3 in 2° bins for 2011.

usually near 20 cm. The bias of the orbital wave velocity (*Vorb*) derived from the azimuth cutoff is given in the top-right plot. Here equation (1) is used to convert the azimuth cutoff to orbital wave velocity which is the second moment of the wave spectrum. The comparison is reasonable with errors less than 2 cm/s. The wave height biases have a similar pattern as the orbital wave velocities in the low latitudes (<30°N/S) Pacific and Indian Oceans. This suggests the errors in *Hs* ($\sim m0$) are causing the differences in $m2$. Therefore it is expected that the ratio between the two, which is approximately the average wave period ($Tm02$), is minimal. Some regions do not have the same *Hs* and *Vorb* biases like the region south of Australia, the Northeast Pacific, and the Northwest Atlantic. The disparity between the wind waves and swell is most likely causing these differences. One possible explanation is that in the wind wave component in the Northwest Atlantic is too strong compared to the swell. On the other hand, in the Northeast Pacific and south of Australia the swell component is too strong compared to the wind waves. In this global implementation of the WW3, we do not include currents and likely introduces errors.

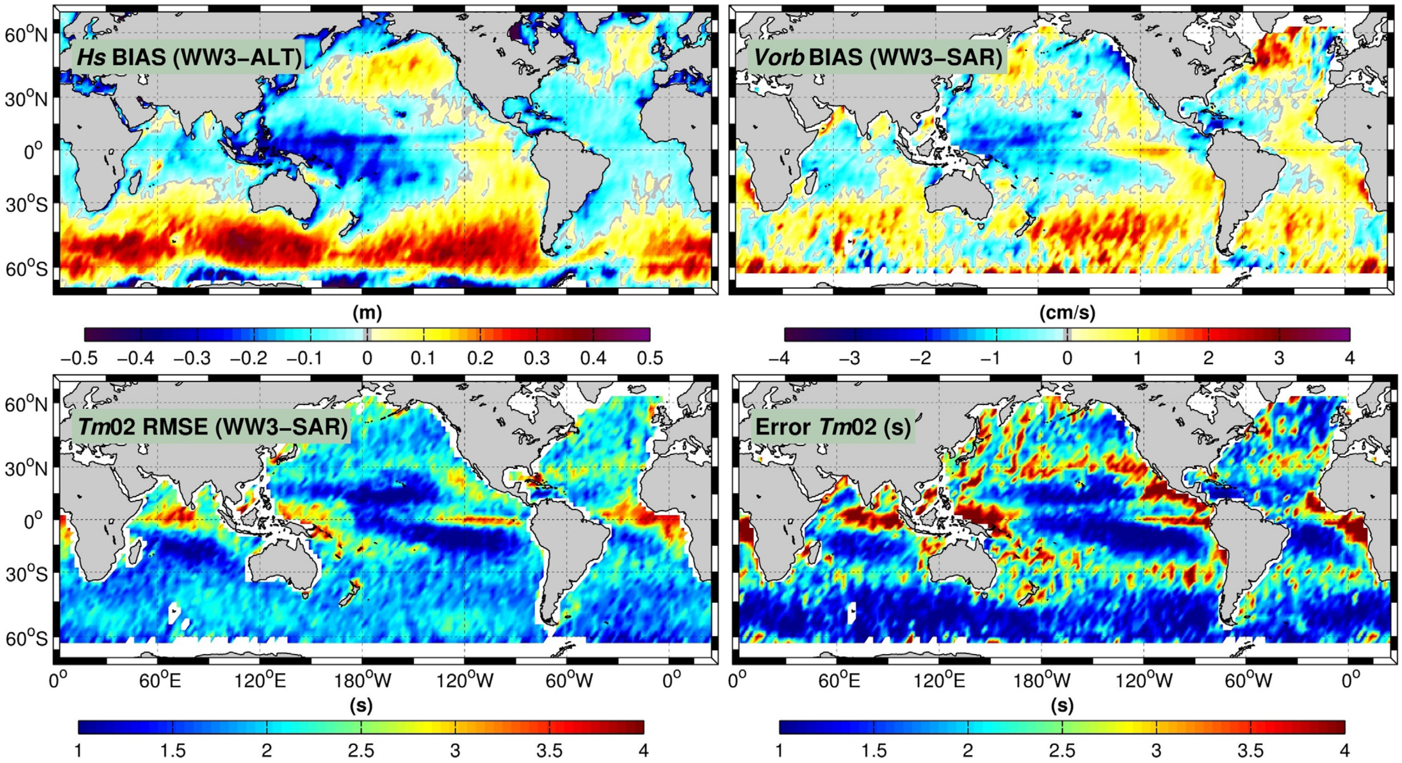

Figure 10. (top-left) Significant wave height (*Hs*) bias (WW3-Alimeter), (top-right) wave orbital velocity (*Vorb*) bias WW3-SAR, (bottom-left) root mean square error of the average wave period (*Tm*02) colocating the significant wave height from the altimeter and the orbital wave velocity from SAR for 2011. (bottom-right) Error propagation of the significant wave height and orbital wave velocity to the average wave period assuming the quantities are independent for 2011.

The square root of the ratio of *m*0 and *m*2 gives the average wave period which has not been validated as extensively as the *Hs*. The altimeter is directed in the nadir direction while the SAR is directed 23° from nadir therefore the sensors do not measure the same ocean conditions. Based on ENVISAT's altitude their distances can be 200–300 km from each other. This approximation in the extra tropics (>30°N/S) will induce errors since the wave conditions change more rapidly than the tropics (<30°N/S). Nevertheless we consider the closest altimeter observations to the SAR measurement and compare the average wave period to WW3. The bottom-left plot shows the root mean square errors are normally 2 s with higher discrepancies near the Equator. To complement this analysis we assume the *m*0 and *m*2 are independent and propagate the error to *Tm*02 as shown in the bottom-right plot. These results are surprisingly similar. WW3 might have some spatial and/or timing errors related to the CFSR forcing since higher errors at the boundary between the Westerlies ~30°N/S is clear. Other than that the largest errors occur near the Equator adjacent to land masses and might be related to currents or small scale dynamics not resolved by the global implementation of WW3. It is expected there are systematic errors in the SAR data related to other physical processes like atmospheric pressure fronts or strong changes in ocean temperature. Therefore the SAR/WW3 discrepancies in these areas are difficult to diagnose.

4.2. Wave Climate

The wave climate is described utilizing the 10 years of ENVISAT derived wave orbital velocity. The quantity can be thought of as a significant wave orbital velocity that mainly resolves the wind waves. Figure 11 displays the seasonal averages grouped in 3 month blocks: December–January–February (DJF), March–April–May (MAM), June–July–August (JJA), and September–October–November (SON). For reference the seasonal-averaged colocated significant wave heights from WW3 are given in Figure 12. DJF has a maximum *Vorb* in the North Pacific and North Atlantic around 50°N, while the activity in the Southern Hemisphere is at its minimum. The North Pacific trade winds have a distinct feature extending to China. This is contrary to the fact that the Easterly winds are generally less persistent this time

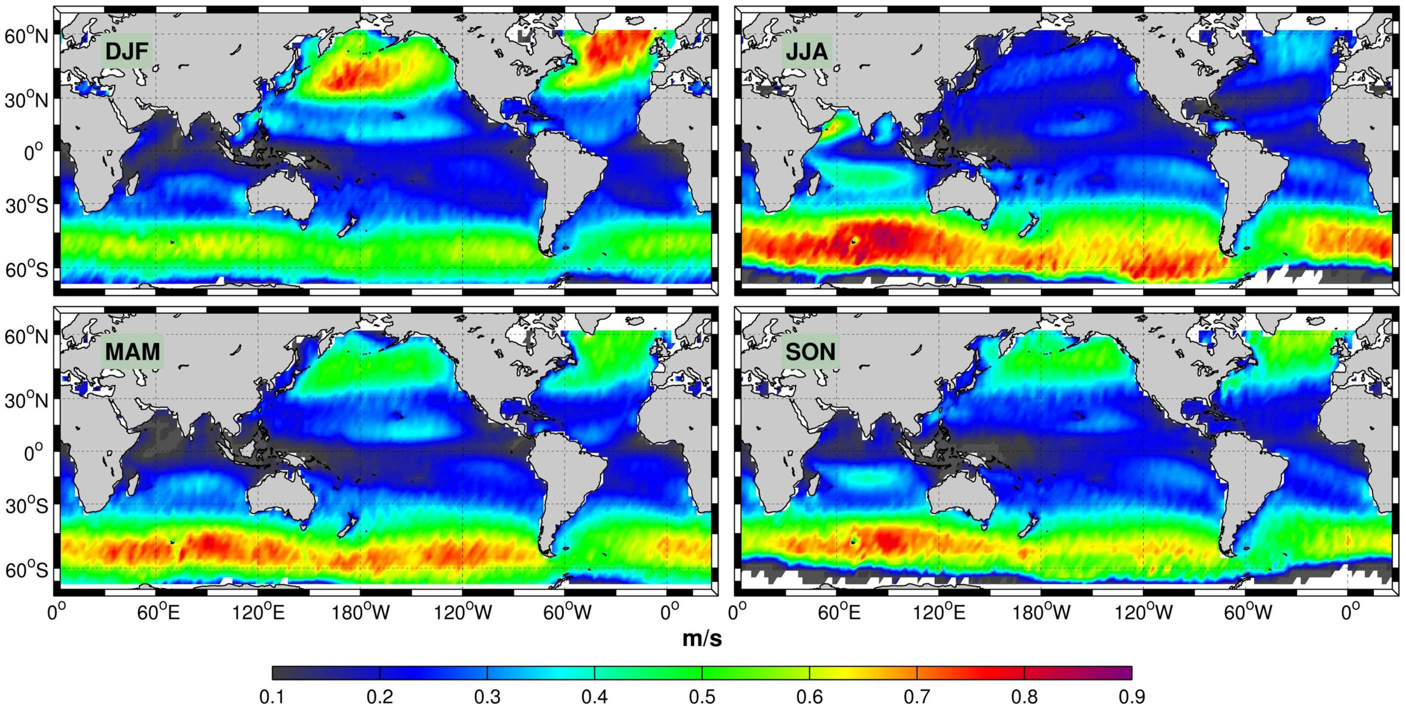

Figure 11. Wave orbital velocity seasonal averages using ENVISAT SAR 2002–2012 for December–January–February (DJF), March–April–May (MAM), June–July–August (JJA), and September–October–November (SON).

of year [*Stopa et al.*, 2013a]. This feature also persists into MAM but it is weaker in magnitude and does not extend to the Western Pacific. The wave orbital velocities in the North Pacific and North Atlantic reduce, while in the Southern Hemisphere they are enhanced and some moderate velocities

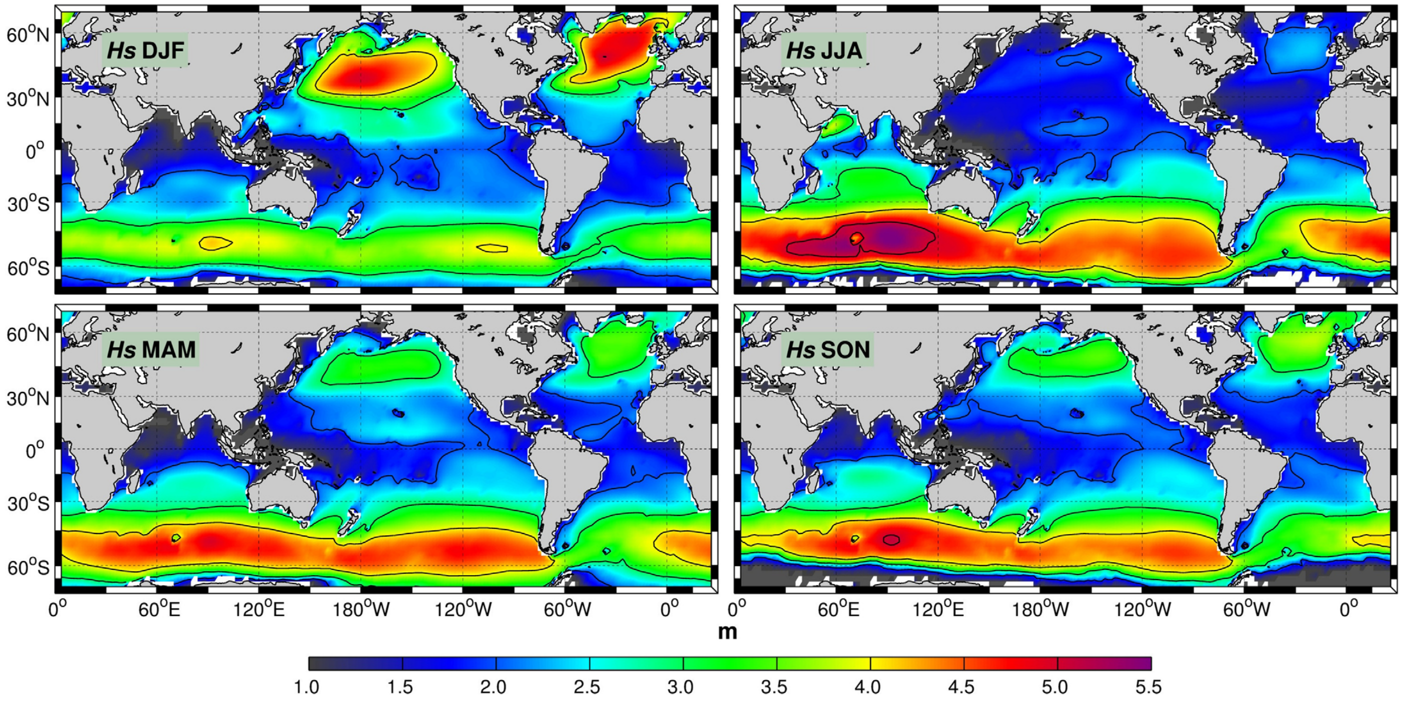

Figure 12. Significant wave height seasonal average using WW3 data that correspond to the ENVISAT observations 2002–2012 for December–January–February (DJF), March–April–May (MAM), June–July–August (JJA), and September–October–November (SON).

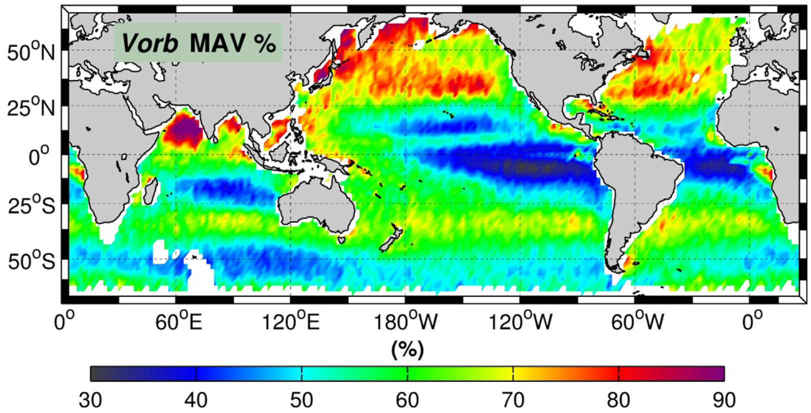

Figure 13. Wave orbital velocity mean annual variability (MAV = $\overline{\sigma_j/\overline{x_j}}$).

(> 0.35 m/s) extend beyond 30°S. JJA has a minimum in the Northern Hemisphere, while Southern Hemisphere reaches its maximum exceeding 0.8 m/s for the majority of the band near 55°S. These are the largest and most consistent velocities with the local maximum observed in the Indian Ocean sector near Kerguelen, which exceed 0.75 m/s for all seasons. The Southern Hemisphere extra tropics are very consistent with regular wave velocities exceeding 0.5 m/s throughout the year. The Arabian Sea in the North Indian Ocean has a maximum in JJA related to the monsoon. The Indian Ocean trade winds that extend from Western Australia to Madagascar (60–110°E, 5–30°S) are enhanced during JJA. SON is similar to MAM with characteristics of both extreme seasons JJA and DJF.

The seasonally averaged wave velocities are representative of wind waves with zonal patterns of the global circulation having the most prominent features in the extra tropics (30–60°N/S). Qualitatively the wave orbital velocities match the spatial pattern of the seasonal wave heights in Figure 12. The wave orbital velocities are more influenced by smaller scales therefore the generation regions have slightly sharper contrast. The effect of swell also convolutes the wave heights making the transition into in tropics (<30°N/S) more gradual. Since the *Hs* (*m*0) and *Vorb* (*m*2) behave similarly, it is feasible to approximate the wind sea (or total) significant wave height empirically much like *Tm*02 is approximated from σ_0 (equivalent to *m*4) [*Gommenginger et al.*, 2003]. Comparing *Vorb* to the wind speed seasonal averages of CFSR presented by *Stopa et al.* [2013b], the orbital wave velocity better isolates the important wave generation regions associated with developing seas. This is consistent with *Semedo et al.* [2011] who used ERA-40 to describe the climate through the separation of wind waves and swells. The extra tropics are the dominate source of generation while the low latitudes (<30°N/S) are relatively calm. However the noted sources in the Indian Ocean (10–30°S) and North Pacific (10–30°N) trade wind regions produce prominent features with velocities of 0.35 m/s.

It is clear that the Northern Hemisphere has a larger change in seasonality and this is quantified by the mean annual variability (MAV = $\overline{\sigma_j/\overline{x_j}}$) in Figure 13. This metric is the average of each year *j*'s standard deviation normalized by the annual average. The Northern Hemisphere extra tropics have the largest seasonal extremes exceeding the 80% level. On the other hand, the Southern Hemisphere extra tropics centered at 50°S is relatively consistent and deviates less than 50% throughout the year. The northern edge of this region demonstrates an enhanced variability of 60% representative of the expanded storm region of JJA. The highest peaks are located in the Western Pacific near Japan and in the Indian Ocean near India. The Indian monsoon region extends through the Philippines. The persistent trade wind region of the South Pacific extends across the Equator and has the lowest variability of any region deviating less than 35% per year (centered near 125°W, 10°S). The consistent trade winds all have minima centered in the respective oceans: North Pacific (160°W,15°N), Indian Ocean (75°E,15°S), and South Atlantic (30°E,10°S). Despite the relatively weak wave velocities in the Gulf of Mexico and seas near Indonesia, the annual variability is very sensitive to changes in wave velocities resulting in higher values of MAV.

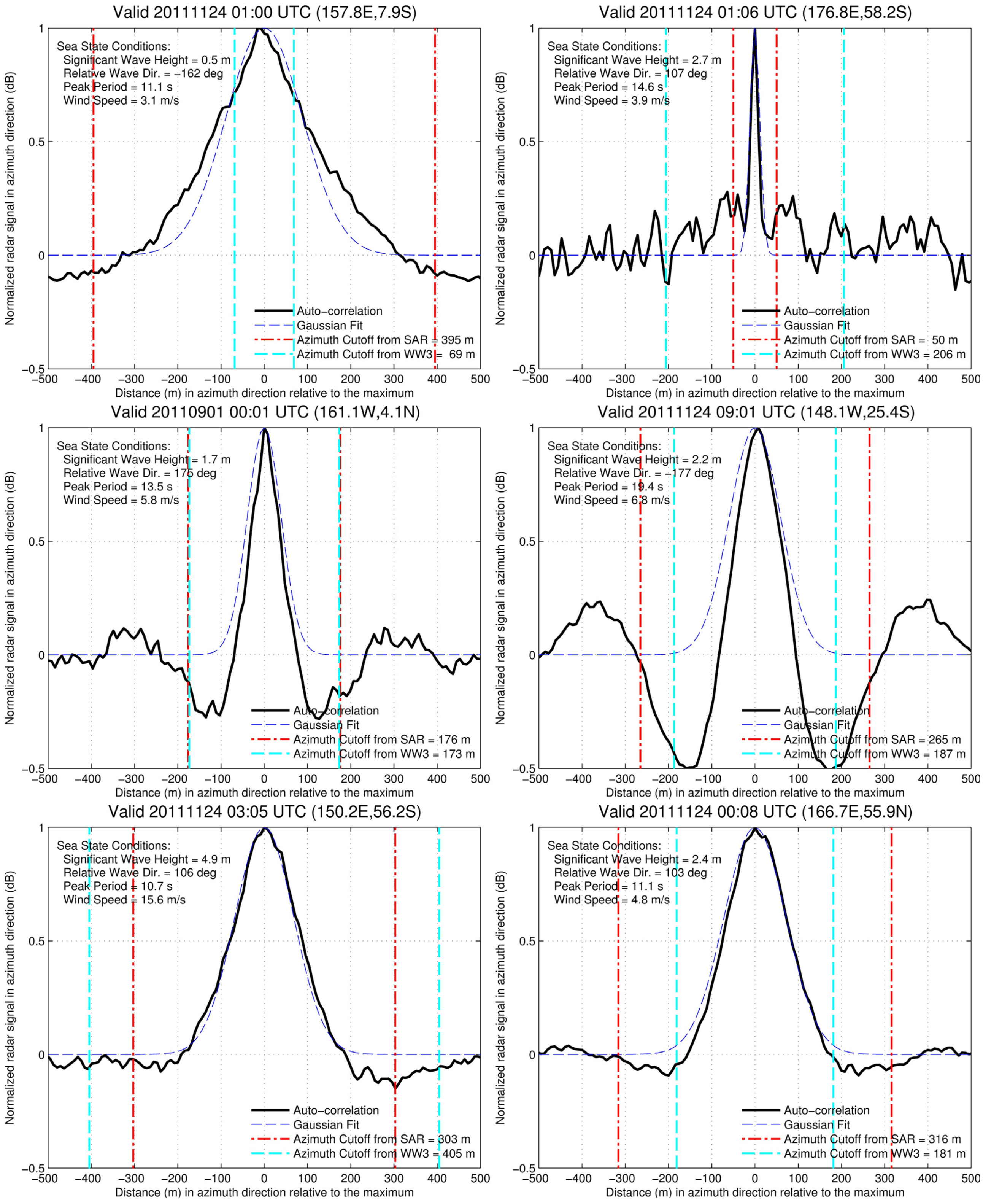

Figure 14. Representative examples of the azimuth cutoff estimation demonstrating some of the larger errors. Solid black line represents the auto-correlation function of the maximum pixel along the azimuth direction, the dashed blue line represents the Gaussian fit, the red vertical dash-dot line is the cutoff estimated from SAR, and the cyan vertical dashed line is the cutoff estimated from WW3. The wind and dominant wave conditions are given in the top-left corner of each plot. (top) Examples when the wind is calm. (middle) Representative examples of the azimuth cutoff estimation when the waves are directed along the satellite track. (bottom) Examples of under/over estimation of the azimuth cutoff when the waves are directed in the range direction.

In summary, the derived orbital velocities from ENVISAT ASAR are consistent with previous climate studies and offer a new perspective on the wave climate by highlighting the wave generation regions.

5. Discussion and Conclusions

The azimuth cutoff measured from SAR is related to the wave orbital velocity to provide a useful quantity of remotely sensed sea state information. We perform rigorous comparisons with directional wave buoys and WW3. The SAR derived wave orbital velocities have the same accuracy in deep and shallow waters making it applicable to many practical engineering issues in both near-shore and offshore locations. In general, the parameter performs well but systematic biases are clear and occur under the smallest ($<$ 100 m) and largest sea states ($>$ 400 m) with a strong relationship to the wind speed. In order to summarize the different errors, Figure 14 shows examples of the auto-correlation and the fitted Gaussian curve along the azimuth direction. For reference the azimuth cutoff from WW3 is given to show the discrepancies.

From Figure 4 and Table 1, it is observed that there is often overestimation of the azimuth cutoff when the wind speed is calm ($<$ 3m/s) and the wave height is small, before the empirical correction. The top-left plot shows an example when the cutoff is drastically overestimated. Under these conditions, there might not be enough sea surface roughness to create the required contrast to properly resolve the scene, resulting in a triangular shaped auto-correlation function. The Gaussian fit is able to adequately capture the shape but the algorithm considerably overestimates the cutoff. The empirical bias correction is heavily weighted on the wind speed and helps improve the performance of the azimuth cutoff for these events. Although this is not common, incoherent autocorrelation functions can exist like the example in the top-right plot. The algorithm drastically underestimates the cutoff in this example composed of calm winds and a swell directed in the range direction. The Gaussian shape matches the center portion of the auto-correlation function but modeling the outer limits of the auto-correlation is difficult and results in an underestimation.

Figure 5 shows that the errors are reduced when waves are directed along the azimuth direction compared to the range. This is counter-intuitive because it is expected that the algorithm would have difficulty in accurately describing the cutoff along the track since the waves are contained within the auto-correlation. The examples in the middle plots show that the waves directed along the satellite track dominate the shape of the auto-correlation and results in a sinc-shaped function. However, the algorithm on average performs reasonably well under these conditions (Figure 5). An example of an agreeable match is shown in the middle-left plot while the middle right plot shows larger errors can occur. Notice that as the strength of the swell increases (wave height and period), the energy in the side lobes increases making the truncation of the standard error more difficult. When waves are traveling in the near range direction there is a larger variability of the cutoff residuals (Figure 5). Even when the fit appears to be reasonable like the bottom plots, the cutoff can be over/under-estimated by 100 m. The standard error between the Gaussian and the auto-correlation might not be sensitive enough to determine the truncation point. The bottom-left plot is a representative example of the underestimation seen when the waves are taller and the winds are stronger. On the other hand, the bottom-right plot is a more common representation and creates the positive bias like observed in Figure 5. Since the azimuth cutoff is used as a proxy for the wave energy not resolved by the SAR, an improved performance will result in more accurate wave spectra and directly affect the accuracy of the partitioned wave quantities.

Systematic biases of the azimuth cutoff are seen in both buoy and SAR quantities with a strong relationship to the wind speed, significant wave height and mean squared slope. In order to improve the performance we use a multivariate regression of the SAR derived quantities from the radar signal: sigma naught, wind speed, and normalized variance. This correction removes the bias but does not completely remove the errors like the examples in Figure 14. One application of this empirical fit is the ability to assess the quality of the recorded SAR images. For example, if the empirical correction is a large proportion of the Gaussian fit estimate the SAR image might not be well resolved and the cutoff should be flagged as poor quality.

In the future, other empirical nonlinear methods, similar to the geophysical model functions developed to estimate wind speeds, can be created to estimate the azimuth cutoff. Nonlinear behavior of the cutoff residual is seen with respect to significant wave heights and mean-squared slopes showing the fine details of the wave field are not well resolved. While there are some obvious spatial errors, SAR and WW3 are strongly correlated with small scatter indices demonstrating the azimuth cutoff is a robust estimator under the majority of wave conditions.

As an application, the wave orbital velocities are used to diagnose WW3. The spatial comparison of the wave orbital velocities between SAR and WW3 reveal some of the biases can be related to errors in the significant wave height. However, disparities occur and are related to the improper balance of growth and dissipation or could be related to the discrete interaction approximation (DIA) of nonlinear energy transfer within the wave spectrum [*Hasselmann et al*., 1985b]. There is less validation of higher order wave moments from WW3, so we make use of the high spatial coverage to compare the average wave period using two different techniques. The spatial pattern is very similar suggesting coherence between the methods. However, the magnitude of the errors should be taken with caution since they are higher than established errors from in-situ buoys which yielded errors less than 0.5 s [*Stopa et al*., 2015].

The wave orbital velocities derived from SAR offer some insights to the wave climate since the parameter isolates the wind seas. For example, the North Pacific tropics have a discernible region that extends to the western Pacific in the boreal winter months. The trade winds are less persistent this time of year, but this discernible feature might be reflective of higher episodic events previously not well quantified by significant wave heights or wind speeds. The seasonality of *Hs* and *Vorb* are in good agreement, and it is probable that empirical methods could approximate *m*0 from SAR's *m*2 and wave spectrum. Corroborating previous works, the Southern Hemisphere is the most active region due to the unimpeded expanse of ocean [e.g., *Hemer et al*., 2010]. The Northern Hemisphere has stronger seasonal cycle compared to the Southern Hemisphere revealed using the mean annual variability [*Stopa et al*., 2013b].

The SAR also provides meaningful wind information to the scientific community. Much like other remotely sensed winds, the SAR normalized radar cross section responds to sea surface roughness and geophysical model functions are used to estimate wind speeds. This is similar to the routine operations of altimeters and scatterometers [*Vandemark et al*., 1997; *Weissman and Graber*, 1999]. Errors in these derived wind speeds have been related to the presence of surface currents, atmospheric fronts, precipitation, and most importantly the sea state [e.g., *Ebuchi et al*., 2002; *Vandemark et al*., 1997, *Quilfen et al*., 2001]. This has sparked the development of improved empirical relationships that use the radar cross section and sea state information for both Ku-band altimeters by *Gourrion et al*. [2002] and C-band scatterometers by *Quilfen et al*. [2004a, 2004b]. We demonstrate here, that azimuth cutoff estimated from the radar signal along the azimuth direction, can be used as a proxy for the orbital velocity of the waves not fully resolved by the SAR imaging. Therefore, for low incidence angles, it is feasible to use the azimuth cutoff along with sigma naught to improve the geophysical model functions and create a more accurate SAR wind speed.

The impact of remotely sensed observations continually shapes our understanding of the Earth's dynamics providing large spatial coverage. The recorded backscattered power of SAR contains a plethora of sea-state information. The wave mode on ENVISAT has been designed to best resolve the large scale swells [e.g., *Husson et al*., 2012]. In this study we demonstrate wave orbital velocities can be estimated indirectly through the SAR processing which gives an indication of the waves unresolved by the SAR images. As it follows the azimuth cutoff proportional to the root mean square surface orbital wave velocity provides additional information about the sea state. With the newly available Sentinel-1 measurements, it is encouraging to make better use of the SAR measurements for practical applications, further building on the near continuous 10 years of ENVISAT to demonstrate the value of long-term observations.

The wave orbital velocities presented here are an important parameter for ocean engineering applications and can be used as a reference or an acceptance range to constrain wave models or oceanography studies.

Acknowledgments

This work was supported by the "Laboratoire d'Excellence" LabexMER (ANR-10-LABX-19), cofunded by a grant from the French government under the program "Investissements d'Avenir," and Regional Council of Brittany (SAD program). The ENVISAT SAR data sets are made available through the European Space Agency through the GlobWAVE project (http://globwave.ifremer.fr/) and the buoy data sets are available from the National Data Buoy Network (www.nodc.noaa.gov/BUOY/) and the Coastal Data Information Program (https://cdip.ucsd.edu/). We would like to thank the two anonymous reviewers for their comments that have improved this paper.

References

Alpers, W. B., and C. Bruning (1986), On the relative importance of motion-related contributions to the SAR imaging mechanism of ocean surface waves, *IEEE Trans. Geosci. Remote Sens.*, *24*(6), 873–885.

Alpers, W. B., D. B. Ross, and C. L. Ruffenach (1981), On the detectability of ocean surface waves by real and synthetic aperture radar, *J. Geophys. Res.*, *86*(C7), 6481–6498.

Alves, J. H. G. M., M.L. Banner, and I. R. Young (2003), Revisiting the Pierson-Moskowitz asymptotic limits for fully developed wind waves, *J. Phys. Oceanogr.*, *33*, 1301–1323.

Ardhuin, F., et al. (2010), Semi-empirical dissipation source functions for ocean waves. Part I: Definition, calibration, and validation, *J. Phys. Oceanogr.*, *40*(9), 1917–1941.

Ardhuin, F., J. Tournadre, P. Queffeulou, F. Girard-Ardhuin, and F. Collard (2011), Observation and parameterization of small icebergs: Drifting breakwaters in the southern ocean, *Ocean Modell.*, *39*, 405–410.

Ardhuin, F., F. Collard, B. Chapron, F. Girard-Ardhuin, G. Guitton, A. Mouche, and J. E. Stopa (2015), Estimates of ocean wave heights and attenuation in sea ice using the SAR wave mode on Sentinel-1A, *Geophys. Res. Lett.*, *42*, 2317–2325, doi:10.1002/2014GL062940.

Beal, R. C., D. G. Tilley, and F. M. Monaldo (1983), Large and small-scale spatial evolution of digitally processed ocean wave spectra from Seasat synthetic aperture radar, *J. Geophys. Res.*, *88*(C3), 1761–1778.

Chapron, B., H. Johnsen, and R. Garello (2001), Wave and wind retrieval from SAR images of the ocean, *Ann. Telecommun.*, *56*, 682–699.

Chawla, A., and H. L. Tolman (2008), Obstruction grids for spectral wave models, *Ocean Modell.*, *22*(1-2), 12–25.

Chen, G., B. Chapron, R. Ezraty, and D. Vandemark (2002), A global view of swell and wind sea climate in the ocean by satellite altimeter and scatterometer, *J. Atmos. Oceanic Technol.*, *19*(11), 1849–1859.

Collard, F., F. Ardhuin, and B. Chapron (2005), Extraction of coastal ocean wave fields from SAR images, *IEEE J. Oceanic Eng.*, *30*(3), 526–533.

Collard, F., F. Ardhuin, and B. Chapron (2009), Monitoring and analysis of ocean swell fields from space: New methods for routine observations, *J. Geophys. Res.*, *114*, C07023, doi:10.1029/2008JC005215.

Earle, M. D., K. E. Steele, and D. W. C. Wang (1999), Use of advanced directional wave spectra analysis methods, *Ocean Eng.*, *26*, 1421–1434.

Ebuchi, N., H. C. Graber, and M. J. Caruso (2002), Evaluation of wind vectors observed by QuikSCAT/SeaWinds using ocean buoy data, *J. Atmos. Oceanic Technol.*, *19*(12), 2049–2062.

Elfouhaily, T., B. Chapron, K. Katsaros, and D. Vandemark (1997), A unified directional spectrum for long and short wind-driven waves, *J. Geophys. Res.*, *102*(C7), 15,781-15,796.

Gommenginger, C. P., M. A. Srokosz, and P. G. Challenor (2003), Measuring ocean wave period with satellite altimeters: A simple empirical model, *Geophys. Res. Lett.*, *30*(22), 2150, doi:10.1029/2003GL017743.

Gourrion, J., D. Vandemark, S. Bailey, B. Chapron, C. P. Gommenginger, P. G. Challenor, and M. A. Srokosz (2002), A two parameter wind speed algorithm for Ku-band altimeters, *J. Atmos. Oceanic Technol.*, *19*, 2030–2048.

Hasselmann, K., R. K. Raney, W. J. Plant, W. Alpers, R. A. Shuchman, D. R. Lyzenga, C. L. Rufenach, and M. J. Tucker (1985a), Theory of synthetic aperture radar ocean imaging: A MARSEN view, *J. Geophys. Res.*, *90*(C3), 4659–4686.

Hasselmann, S., K. Hasselmann, J. H. Allender, and T. P. Barnett (1985b), Computations and parameterizations of the nonlinear energy transfer in a gravity-wave spectrum. Part II: Parameterizations of the nonlinear energy transfer for application in wave models, *J. Phys. Oceanogr.*, *15*(11), 1378–1391.

Hemer, M. A., J. A. Church, and J. R. Hunter (2010), Variability and trends in the directional wave climate of the Southern Hemisphere, *Int. J. Climatol.*, *30*(4), 475–491.

Husson, R., F. Ardhuin, F. Collard, B. Chapron*, and* A. Balanche (2012), Revealing forerunners on Envisat's wave mode ASAR using the Global Seismic Network, *Geophys. Res. Lett.*, *39*, L15609, doi:10.1029/2012GL052334.

Kerbaol V., B. Chapron and P. Vachon (1998), Analysis of ERS-1/2 synthetic aperture radar wave mode imagettes, *J. Geophys. Res.*, *103*(C4), 7833–7846.

Longuet-Higgins, M. S. (1952), On the statistical distributions of sea waves, *J. Mar. Res.*, *11*, 245–265.

Lyzenga, D. R. (1986), Numerical simulation of synthetic aperture radar image spectra for ocean waves, *IEEE Trans. Geosci. Remote Sens.*, *24*(6), 863–872.

Pierson, W. J., and L. Moskowitz (1964), A proposed spectral form for fully developed wind seas based on the similarity theory of S. A. Kitaigorodskii, *J. Geophys. Res.*, *69*(24), 5181–5190.

Portilla, J., F. J. Ocampo-Torres and J. Monbaliu (2009), Spectral partitioning and identification of wind sea and swell, *J. Atmos. Oceanic Technol.*, *26*, 107–122.

Queffeulou, P., and D. Croizé-Fillon (2015), Global altimeter SWH data set, version 11.1, September. Tech. rep. 11.1, IFREMER, Plouzane, France. [Available at ftp://ftp.ifremer.fr/ifremer/cersat/products/swath/altimeters/waves/documentation/altimeter_wave_merge__11.1.pdf.]

Quilfen, Y., B. Chapron, and D. Vandemark (2001), The ERS scatterometer wind measurement accuracy: Evidence of seasonal and regional biases, *J. Atmos. Oceanic Technol.*, *18*, 1684–1697.

Quilfen, Y., B. Chapron, F. Collard, and D. Vandemark (2004a), Relationship between ERS scatterometer measurement and integrated wind and wave parameters, *J. Atmos. Oceanic Technol.*, *21*(2), 368–373.

Quilfen Y., B. Chapron, F. Collard, and M. Serre (2004b), Calibration/validation of an altimeter wave period model and application to TOPEX/Poseidon and Jason-1 altimeters, *Mar. Geod.*, *27*(3-4), 535–549.

Rascle, N., and F. Ardhuin (2013), A global wave parameter database for geophysical applications. Part 2: Model validation with improved source term parameterization, *Ocean Modell.*, *70*, 174–188.

Saha, S., et al. (2010), The NCEP climate forecast system reanalysis, *Bull. Am. Meteorol. Soc.*, *91*, 1015–1057.

Saha, S., et al. (2014), The NCEP climate forecast system version 2, *J. Clim.*, *27*(6), 2185–2208.

Semedo, A., K. Suselij, A. Rutgersson, and A. Sterl (2011), A global view on the wind sea and swell climate and variability from ERA-40, *J. Clim.*, *24*(5), 1461–1479.

Sepulveda, H. H., P. Queffeulou, and F. Ardhuin (2015), Assessment of SARAL AltiKa wave height measurements relative to buoy, Jason-2 and Cryosat-2 data, *Mar. Geod.*, *38*, 449–465, doi:10.1080/01490419.2014.1000470.

Stopa, J. E., J.-F. Filipot, N. Li, K. F. Cheung, Y.-L. Chen, and L. Vega (2013a), Wave energy resources along the Hawaiian Island chain, *Renewable Energy*, *55*, 305–321.

Stopa, J. E., K. F. Cheung, H. L. Tolman, and A. Chawla (2013b), Patterns and cycles in the climate forecast system reanalysis wind and wave data, *Ocean Modell.*, *70*, 207–220.

Stopa, J. E., F. Ardhuin, A. V. Babanin, and S. Zieger (2015), Comparison and validation of physical wave parameterizations in spectral wave models, *Ocean Modell.*, doi:10.1016/j.ocemod.2015.09.003.

Swift, C. T., and L. R. Wilson (1979), Synthetic aperture radar imaging of moving ocean waves, *IEEE Trans. Antennas Propag.*, *27*(6), 725–729.

Tolman, H. L. (2003a), Treatment of unresolved islands and ice in wind wave models, *Ocean Modell.*, *5*(3), 219–231.

Tolman, H. L. (2003b), Erratum to "Treatment of unresolved islands and ice in wind wave models" [Ocean Mod. 5(3) (2003) 219-231], *Ocean Modell.*, *5*(4), 381–384.

Tolman, H. L., and the WAVEWATCH III ® Development Group (2014), User manual and system documentation of WAVEWATCH III® version 4.18, *NOAA/NWS/NCEP/MMAB Tech., College Park, Md. Note 316*, 282 pp. + Appendices.

Tucker, M. J. (1985), The imaging of waves by satellite borne synthetic aperture radar: The effect of sea-surface motion, *Int. J. Remote Sens.*, *6*(7), 1059–1074.

Vandemark, D., J. B. Edson, and B. Chapron (1997), Altimeter estimation of sea surface wind stress for light to moderate winds, *J. Atmos. Oceanic Technol.*, *14*, 716–722.

Vandemark, D., B. Chapron, T. Elfouhaily, and J. W. Campbell (2005), Impact of high-frequency waves on the ocean altimeter range bias, *J. Geophys. Res.*, *110*, C11006, doi:10.1029/2005JC002979.

Weissman, D. E. and H. C. Graber (1999), Satellite scatterometer studies of ocean surface stress and drag coefficients using a direct model, *J. Geophys. Res.*, *104*(C5), 11,329–11,335.

Erratum

In the originally published version of this article, the colorbar of Figure 11 was incorrect. There was a factor of pi missing; thus the min and max values should have been approximately 6 to 90 cm/s. In the paper, the authors use the image to qualitatively demonstrate that the satellite derived parameter (root mean square orbital wave velocity) is geophysical. Only the magnitudes have changed due to this correction; otherwise, the text description is the same. Figure 11 and section 4.2 have since been corrected to reflect this adjustment, and this version may be considered the authoritative version of record.